Failure of Hydrided Zircaloy-4 Fuel Cladding Tubes under RIA Loading Conditions

M. Le Saux[1,a], J. Besson[2,b], S. Carassou[1,c], C. Poussard[1,d] and X. Averty[1,e]

[1]CEA-Saclay, DEN/DMN/SEMI, 91191 Gif-Sur-Yvette, France

[2]Centre des Matériaux, Mines Paris, CNRS UMR 7633, BP 87, 91003 Evry, France

[a]matthieu.lesaux@cea.fr, [b]jacques.besson@ensmp.fr, [c]sebastien.carassou@cea.fr, [d]christophe.poussard@cea.fr, [e]xavier.averty@cea.fr

Keywords: Zircaloy-4 fuel cladding, RIA, hydride, viscoplasticity, ductile fracture.

Abstract. The anisotropic viscoplastic behavior and the fracture of cold-worked stress relieved Zircaloy-4 cladding tubes is investigated under reactivity initiated accidents loading conditions. The combined effects of temperature (from 25°C up to 480°C), hydrogen content (from 0 up to 1200 ppm) and stress/stain state (from uniaxial tension up to plane strain tension) are analyzed. A strengthening effect of hydride precipitates and a softening effect of dissolved hydrogen are observed. Ductility of the material increases with increasing temperature and decreases with increasing hydrogen content at room temperature. The embrittlement effect of hydrides is substantially reduced when increasing temperature. A slight effect of stress/strain triaxiality is evidenced. The evolution of material ductility is associated with a change in the macroscopic fracture aspect and the failure mechanisms. A model is proposed to describe the anisotropic viscoplastic behavior of the material.

Introduction

In order to optimize the use of nuclear fuels and improve the management of Pressurized Water Reactors (PWRs), it is planned to progressively extend the discharge burnup of fuel assemblies. This extension would enhance cladding degradation and may increase the likelihood of cladding failure during postulated design basis accidents such as the Reactivity Initiated Accident (RIA). Caused by the inadvertent ejection of a control rod, this scenario leads to an abrupt fuel pellet thermal expansion, which produces a Pellet-Clad Mechanical Interaction (PMCI). This PCMI forces the fuel cladding to deform at high strain rate (typically 1 s^{-1}) under multiaxial tension (axial and hoop components) with a strain path between plane strain hoop tension and equal-biaxial tension [1]. During this early stage of the transient, temperature of the cladding approximately ranges from 350°C up to 600°C. During reactor operation, the metal-water reaction at the fuel cladding outer surface introduces hydrogen into the metal. Hydrogen uptake is commonly identified as a main contributor to limiting the fracture resistance of high burnup fuel claddings during the PCMI stage of RIAs [2]. Once its solubility limit is reached, hydrogen precipitates as δ-hydride platelets and reduces – depending on temperature – ductility of the cladding material [3-6]. Furthermore, it is expected that the stress state influence the mechanical behavior of the hydrided material [3].

The present work addresses the characterization and the modeling of the combined effects of hydrogen, temperature and stress/strain state on both the viscoplastic behavior and the failure of Zircaloy-4 fuel claddings under RIA loading conditions.

Experiment

Material. The material of this study is Cold-Worked Stress Relieved Zircaloy-4 tube, which is commonly used for fuel claddings in french PWRs. Its chemical weight composition is 1.3% Sn,

0.21% Fe, 0.11% Cr, 0.128% O, Zr balance. The outer diameter and the thickness of the cladding were about 9.5 mm and 0.57 mm, respectively. Microstructure of the material is characterized by elongated grains along the rolling direction (about 10-20 μm long in the rolling direction and 2-5 μm wide in the transverse direction), which corresponds to the tube axial direction. Due to its elaboration processing, the material exhibits a strong crystallographic texture with a majority of basal poles oriented at about ±30° from the tube radial direction.

Tubes have been artificially hydrided at 400°C in an argon/hydrogen mixture, then slowly cooled down (2°C/min) to allow the precipitation of stable δ-hydrides ($ZrH_{1.53}$ to $ZrH_{1.66}$). Nominal hydrogen contents of about 400, 800 and 1200 ppm were obtained, depending on exposure time. The δ-hydrides precipitate as fine platelets both intergranular and transgranular. Stack of these microscopic hydride platelets forms macroscopic hydrides (50 to 200 μm long and 0.3 to 0.6 μm wide) predominantly oriented along the circumferential-axial plane (Fig. 1).

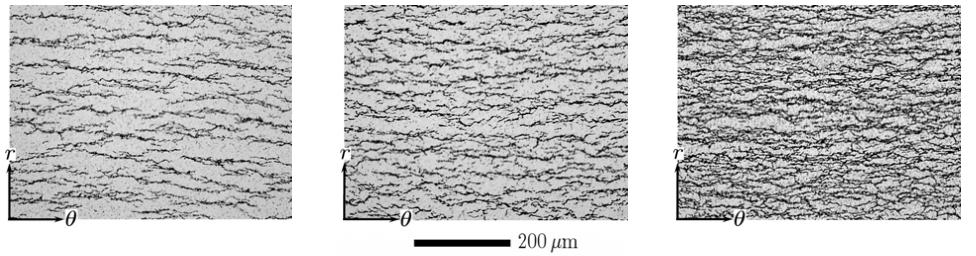

(a) (b) (c)

Fig. 1. Hydride distribution in the material hydrided at (a) 400 ppm, (b) 800 ppm and (c) 1200 ppm.

Mechanical testing. In order to characterize the anisotropic plastic behavior of the material, *Axial Tensile* (AT) and *Hoop Tensile* (HT) tests have been performed using geometries developed in the field of the PROMETRA (TRAnsient MEchanical PROperties) program [1]. The AT specimen is 58 mm long with two 15 mm long and 3 mm wide gauges. The specimen is stretched by pins attached to the cross-head. The HT specimen consists of a 5 mm large small ring with two gauges of 3 mm length and 2 mm width. The sample is placed around two half-cylinder inserts attached to the cross-heads and pulled apart inside the ring. Engineering strain and engineering stress were respectively calculated by dividing the cross-head displacement by the specimen initial gauge length and the applied force by the specimen initial cross-section, s_0. Yield stress at 0.2% plastic strain, $S_Y^{0.2\%}$, maximum stress, S_U, and uniform elongation (plastic strain at S_U), e_U, were determined on the engineering stress-strain curves. In order to characterize ductility of the material, the cross-section reduction, $Z = \Delta s / s_0$, has been optically measured after fracture of the specimens.

In order to study the material failure under loading conditions representative of PCMI (and resulting in similar fracture features) and analyze the influence of the stress/strain state on material ductility, hoop *Plane Strain Tensile* (PST) experiments have been carried out. The wide double edge-notched ring specimen proposed in [7] was used to achieve a plane strain tensile loading in the middle of the specimen. The specimen consists of a 12 mm long ring with two 6.4 mm wide gauge sections flanked by 2 mm diameter notches. Contrary to the configuration proposed in [7], the four notches were oriented perpendicularly to the pulling direction in order to minimize friction effects.

Specimens were tested up to fracture at 25°C, 350°C and 480°C under a constant displacement rate chosen so that the strain rate is about 0.1 s^{-1} within the specimen gauges. Once reached, the target temperature is maintained for about one hour so that the thermodynamical equilibrium condition for the hydrogen/Zircaloy system is almost established before testing. After testing, fracture surfaces were observed by Scanning Electron Microscope (SEM) fractography.

Mechanical behavior

Tests results. As shown in Fig. 2, the flow stress of the material decreases with increasing temperature T. Furthermore, it can be shown that the instantaneous strain hardening exponent of the material, $n = \partial \ln \sigma / \partial \ln p$, depends on plastic strain and decreases like e_U with increasing temperature. At room temperature, S_U linearly increases with increasing hydrogen content, whereas the influence of hydrogen on $S_Y^{0.2\%}$ is lower. This mechanical strengthening is commonly attributed to a composite reinforcement caused by hydrides [4,8]. In accordance with mechanical strengthening, e_U slightly decreases with increasing hydrogen content. At 350°C and 480°C, as hydrogen content increases, mechanical strength of the material decreases for low hydrogen contents while it increases for higher amounts. According to the results reported in [9], the solubility limit of hydrogen in Zircaloy-4 is negligible at room temperature, 126 ppm at 350°C and 399 ppm at 480°C. As a consequence, the decrease in material strength for low hydrogen contents at 350°C and 480°C is probably due to a softening effect of the dissolved hydrogen [10,11]. The strengthening observed for higher hydrogen contents reflects the contribution of the hardening effect of hydrides, which is however expected to decrease when temperature increases [8,12]. The mechanical behavior of the material is anisotropic. It can be shown that plastic anisotropy is nearly constant from room temperature up to 350°C then evolves when increasing temperature. According to [4], no significant effect of hydrogen on plastic anisotropy is highlighted.

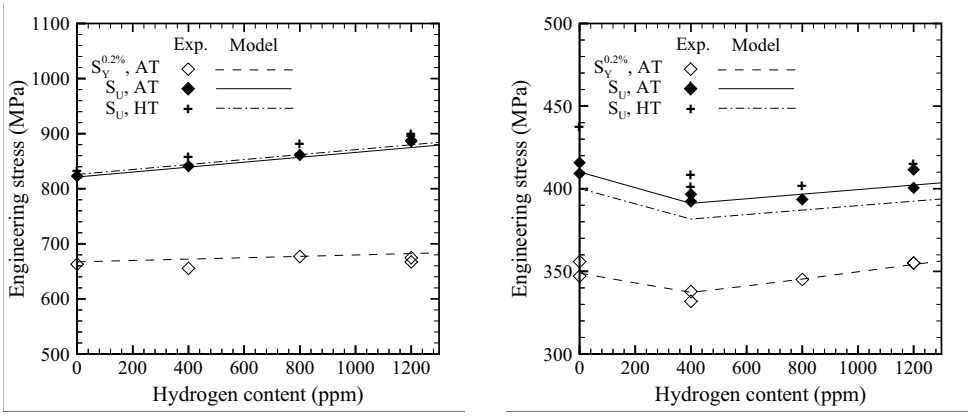

(a) (b)

Fig. 2. $S_Y^{0.2\%}$ and S_U for AT and HT tests performed at (a) 25°C and (b) 480°C.

Modeling. Plastic orthotropy is here described by a Hill's quadratic yield criterion, $\sigma_H(\underline{\sigma}, T) = \sqrt{\underline{\sigma} : \underline{\underline{H}}(T) : \underline{\sigma}}$, where $\underline{\sigma}$ is the stress tensor and $\underline{\underline{H}}$ is a symmetric fourth rank tensor. When expressed in the anisotropy principal axes (r, θ, z), the equivalent stress is written as:

$$\sigma_H = \sqrt{H_{rr}(\sigma_{\theta\theta} - \sigma_{zz})^2 + H_{\theta\theta}(\sigma_{zz} - \sigma_{rr})^2 + H_{zz}(\sigma_{rr} - \sigma_{\theta\theta})^2 + 2H_{r\theta}\sigma_{r\theta}^2 + 2H_{rz}\sigma_{rz}^2 + 2H_{\theta z}\sigma_{\theta z}^2} \quad (1)$$

The Hill coefficients previously identified in [13] are used in the present work to represent the temperature dependent plastic anisotropy.

A multiplicative non linear isotropic hardening model is used to describe the viscoplastic flow of the undamaged material. The viscoplastic strain rate tensor, $\dot{\underline{\varepsilon}}^p$, is obtained by assuming normality:

$$\underline{\dot{\varepsilon}}^{p} = \dot{p}\frac{\partial \sigma_H}{\partial \underline{\sigma}} = \dot{p}\underline{\underline{H}} : \frac{\underline{\sigma}}{\sigma_H}. \tag{2}$$

The equivalent viscoplastic strain rate is given by:

$$\dot{p} = \dot{p}_0 \left(\frac{\sigma_H(T)}{K(T, C_{Hs}, C_{Hp}) L(p, T, C_{Hp})} \right)^{1/m(T)} \tag{3}$$

where m is the strain rate sensitivity coefficient, $\dot{p}_0$ is the reference strain rate fixed to 1s^{-1}, K is the strength coefficient and L is the strain hardening coefficient depending on p. Note that $n = \partial \ln L / \partial \ln p$ under uniaxial loading. According to the experimental results, the strength coefficient K decreases with increasing temperature T and hydrogen in solid solution content C_{Hs} and increases with increasing precipitated hydride content C_{Hp}. The influence of hydrides on K decreases when temperature increases. The strain hardening coefficient L is expressed as a function of plastic strain, temperature and hydride content. In the present work, the tests were performed under only one strain rate. Therefore, the value proposed in [13] for m is used to describe the temperature dependent strain rate sensitivity of the material, which is assumed to be independent on hydrogen content according to [4]. Dissolved and precipitated hydride contents were evaluated from the terminal solubility limit $C_s(T) = 99000 \exp(-34523/RT)$ [9]: $C_{Hs} = \min(C_H, C_s)$ and $C_{Hp} = C_H - C_{Hs}$, where $R = 8.314$ J.mol^{-1}.K^{-1} is the gas constant and C_H is the total hydrogen content. Since no damage was experimentally observed before the onset of necking, the viscoplastic flow law was adjusted without taking into account any coupling with damage. While considering the normalization condition chosen for the determination of Hill coefficients, model parameters were identified using only AT test results. Values of the adjusted parameters are reported in Table 1. As shown in Fig. 2, the model correctly describes the mechanical behavior of the material.

Table 1. Adjusted model parameters (T in K, C_{Hs} and C_{Hp} in ppm).

Elasticity:

$E = 1.059.10^{11} - 36.10^{6} T$, $\nu = 0.342$

Strain rate sensitivity:

$m = 1/[77.68 M_T + 4.11(1 - M_T)]$

where $M_T = 1/[1 + \exp(10.2(T/692 - 1))]$

Plastic anisotropy:

$H_{rr} = 0.485 + 9.5 \cdot 10^{-2} / [1 + \exp(12(T/740 - 1))]$

$H_{\theta\theta} = 1 - H_{rr}$

$H_{zz} = 0.52 + (-0.23 + 4 \cdot 10^{-4} T) / [1 + \exp(15(T/550 - 1))]$

$H_{r\theta} = H_{rz} = H_{\theta z} = 1.5$

Strain hardening:

$L = (p + 1 \cdot 10^{-4})^{n_0} \exp(-\alpha_n p) + (1 - \exp(-\alpha_n p))$

with $n_0 = (1 + 1.45 \cdot 10^{-4} C_{Hp})[4.86 \cdot 10^{-2} N_{0T} + 2.35 \cdot 10^{-2}(1 - N_{0T})]$

where $N_{0T}(T) = 1/[1 + \exp(12(T/(810 - 9.19 \cdot 10^{-2} C_{Hp}) - 1))]$

and $\alpha_n = (53.16 + 1.27 \cdot 10^{-2} C_{Hp})[1 + \exp(11.1(T/738 - 1))]$

Strength:

$K = [1 - 1.175 \cdot 10^{-4} C_{Hs} + (6.15 \cdot 10^{-5} - 4.38 \cdot 10^{-8} T) C_{Hp}][(1.409 \cdot 10^{9} - 8.952 \cdot 10^{5} T) K_T + 4.05 \cdot 10^{7}(1 - K_T)]$

where $K_T = 1/[1 + \exp(1.77(T/1007 - 1))]$

Damage and failure

Tests results. As shown in Fig. 3 (a) and (c), whatever the hydrogen content, ductility of the material during AT and HT tests increases with increasing temperature. At room temperature, Z decreases as hydrogen content increases, demonstrating the embrittlement effect of hydrides. However, failure remains ductile in all cases as it occurred after necking. On the other hand, no significant effect of hydrogen on material ductility is observed at 350°C and 480°C, revealing a reduction of the detrimental effect of hydrides when temperature increases. Z is about 60% higher for HT tests than for AT tests. However, it is difficult to conclude about the anisotropy of damage since failure modes observed during AT and HT tests are not similar.

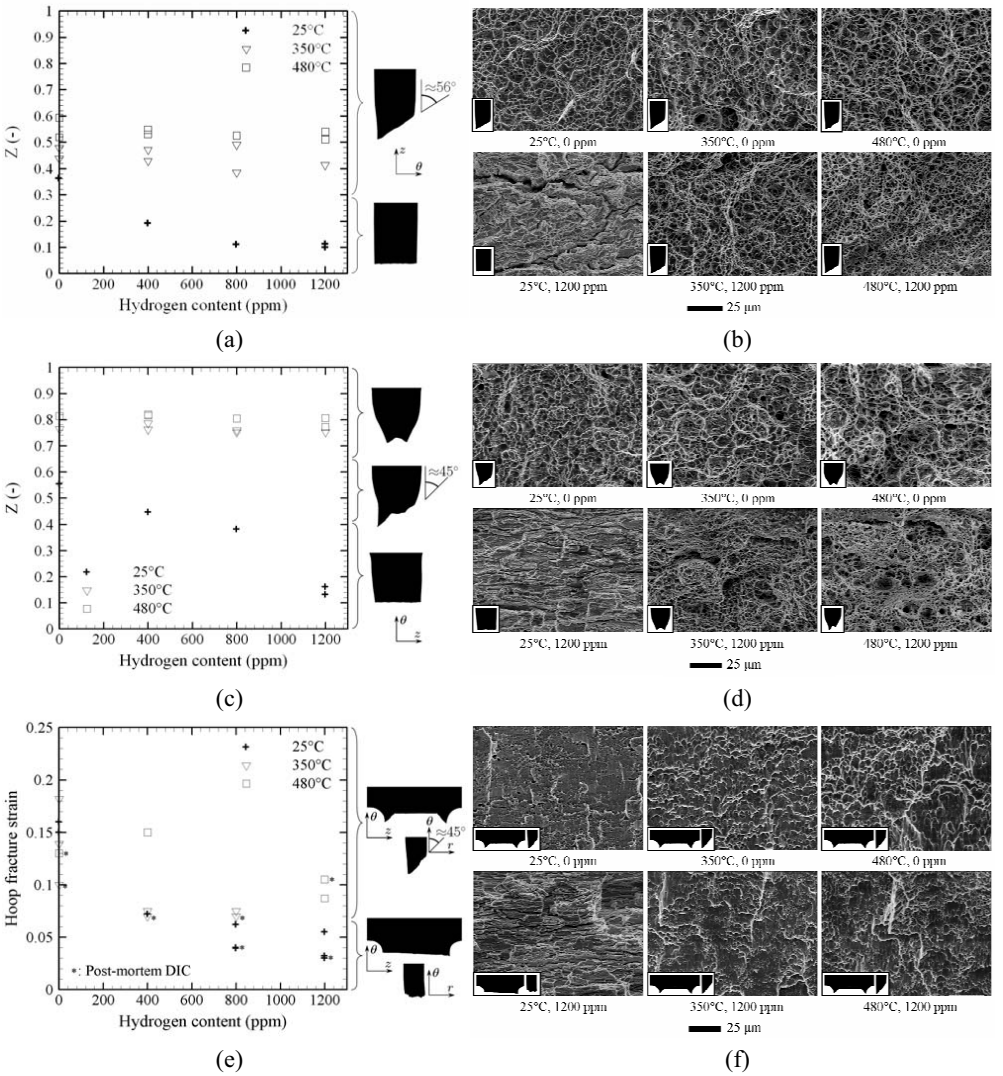

Fig. 3. Z (accuracy ±2%) and fracture surfaces for (a), (b) AT and (c), (d) HT tests. (e) Hoop strain to fracture in the middle of PST specimens outer surface (accuracy ±0.01) and (f) fracture surfaces.

The hoop strains measured on the outer surface at the center of PST specimens by using a 2D Digital Image Correlation (DIC) technique just before failure (*in-situ* DIC) and after failure (*post-mortem* DIC) are shown in Fig. 3 (e). Whereas they provide important information on material ductility, these values should not be rigorously considered as fracture strains since fracture initiated at the center of the specimen inner surface in the case of the material with a significant ductility and at the root of the specimen notches in the case of the hydrided material tested at 25°C. Ductility of the material under PST decreases with increasing hydrogen content at room temperature. On the other hand, no evidence of temperature effect is observed for the non-hydrided material. Despite the accuracy of strain measurements (±0.01) and the experimental scatter, a slight decrease of the fracture strain as a function of hydrogen content may be observed at 350°C. Even considering, according to finite element analysis, that the strain at failure measured on the outer surface of the specimen is nearly two times lower than on the inner surface due in particular to the contact of the specimens with mandrels, fracture strains determined during PST tests appear to be lower than those deduced from HT tests. This suggests that the material ductility depends on the stress/strain state.

Failure mechanisms. In the case of the non-hydrided material whatever the temperature, an inclined localized necking fracture mode at 56° to the loading direction is observed across the width of AT specimens (*slant fracture*). This fracture mode, initiated at the center of the specimen gauge width, is characteristic of plane stress failure in thin specimens. For HT tests, fracture originates after necking in the middle of the specimen gauge section, where the highest stress triaxiality is located. This central crack grows nearly perpendicularly to the loading direction then propagates in the remaining ligaments of the specimen width along localized shear planes at roughly 45° to the specimen axis (*cup-and-cone shaped fracture*). The PST specimens failed due to a through-thickness slip in the plane strain region along a plane inclined at 45° from the cladding thickness (*through-thickness slant fracture*). This fracture mode by shear localization is promoted by the plane strain tension loading and the low strain hardening of the material. Examination of the broken specimens showed that the through-thickness crack initiated on the inner surface of the specimen and propagates along its axial direction. This fracture mode is representative of the PCMI-induced failure observed during RIAs.

At lower scale, SEM fractographies of the non-hydrided specimens show for all testing conditions a ductile fracture aspect with fracture surfaces covered by dimples Fig. 3 (b), (d) and (f). The shape of these dimples depends on the fracture mode. Dimples are rather equiaxed in the case of AT and HT tests. On the other hand, elongated half-voids oriented along the shear direction are observed on the fracture surfaces of PST specimens (combination of normal and shear separation). The hexagonal close-packed C14 Laves phase precipitates $Zr(Fe,Cr)_2$ (diameter of about 200 nm) were observed inside the dimples. Void nucleation is mainly due to particle/matrix interface debonding. For AT and HT tests, void growth is appreciable (due to the increase in stress triaxiality after the onset of necking) and void coalescence occurs by internal necking of intervoid ligaments (Fig. 4 (a)). In the case of PST tests, for which strain localization easily develops into a shear band, void growth is limited and void coalescence rapidly takes place by internal shearing between voids (Fig. 4 (b)).

At room temperature, for the three types of tests, the fracture surface becomes macroscopically plane and perpendicular to the loading direction for the highest hydrogen contents (*flat fracture*). Indeed, fracture of the material embrittled by hydrides occurs prior to the development of localized necking. At 350°C and 480°C, the macroscopic fracture modes are similar to those observed in the case of the non-hydrided material.

As shown in Fig. 3 (b), (d) and (f), large primary voids/secondary cracks perpendicular to the loading direction and corresponding to broken hydrides are clearly visible on the fracture surfaces. As shown in Fig. 5 (a), hydrides (which are aligned along the main tensile loading direction) break due to their negligible ductility at room temperature into several fragments normal to the

macroscopic tension axis. According to a void sheet localization mechanism, the coalescence process involves the formation of large primary voids by hydride cracking subsequently linked by sheets of secondary microvoids probably nucleated at Laves phase particles.

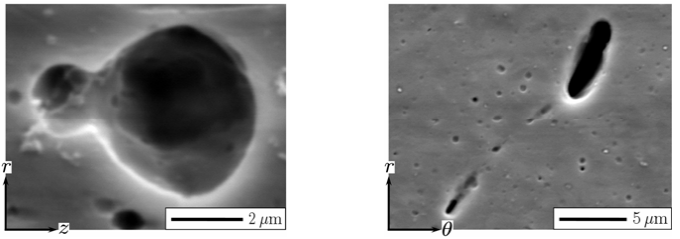

(a) (b)

Fig. 4. Void coalescence by (a) internal necking of intervoid ligaments during an AT test and (b) internal shearing between voids during a PST test.

The hydrides significantly affect the nucleation stage of the damage process, which is therefore dominated by hydride cracking at high hydrogen content. Nearly no broken hydrides are observed on the fracture surfaces of the specimens tested at 350°C and hydride fragmentation disappears at 480°C. This may be attributed to a decrease of the matrix strength and probably an increase of the hydride ductility when increasing temperature [5]. At 350°C and 480°C, dimples are more numerous and smaller for the hydrided material than for the non-hydrided material. Indeed, the reaction of hydrogen with $Zr(Fe,Cr)_2$ precipitates during hydrogen absorption may have embrittled the precipitates and increased their volume [6].

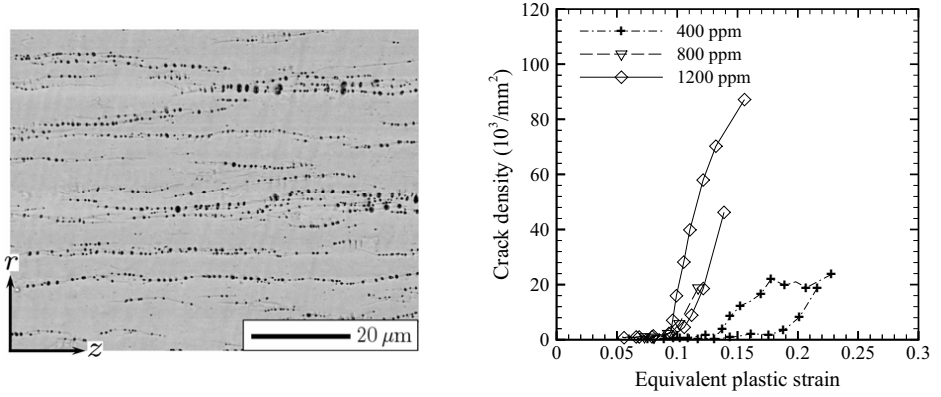

(a) (b)

Fig. 5. (a) Cracked hydrides and (b) crack density (number of cracks per unit area due to hydride cracking as a function of plastic strain for AT tests performed at room temperature ($e_U \approx 0.04$).

Damage kinetics due to hydride cracking. Kinetics of damage caused by hydride cracking at room temperature was quantified by taking advantage of the plastic strain gradient (due to necking) along the loading direction of the broken specimens. Specimens were sectioned after testing in the middle of their width along the loading direction. After polishing and etching, this section was observed using a SEM with a backscattered electron imaging. Damage cartographies were

performed at different distances from the fracture surface (Fig. 5 (a)). Characteristics of voids created by hydride cracking were then determined by using an image processing program. Finally, by correlating these data to the corresponding strain profile, the dependence of void properties on plastic strain was determined. As shown in Fig. 5 (b), damage nucleation starts after necking. This indicates that hydride fracture is preceded by plastic deformation (in accordance with the results reported in [3,4,8]) and that the onset of plastic instability is not influenced by damage. The plastic strain that leads to hydride cracking decreases when increasing hydrogen content.

Conclusions

It is shown that Zircaloy-4 fuel cladding material is reinforced by hydride precipitates and softened by dissolved hydrogen. Ductility of the material increases with increasing temperature. A model is developed to describe the anisotropic viscoplastic behavior of the material. The material is embrittled by hydrides at room temperature. This reduction in ductility diminishes when increasing temperature and becomes insignificant at 350°C and 480°C. A slight decrease in material ductility with increasing stress/strain triaxiality is suggested. Depending on hydrogen content and temperature, damage nucleation occurs by interfacial debonding between matrix and Laves phase precipitates and/or hydride cracking. Void coalescence takes place by internal necking or internal shearing depending on the local stress/strain state.

References

[1] B. Cazalis, J. Desquines, P. Poussard, M. Petit, Y. Monerie, C. Bernaudat, P. Yvon and X. Averty: Nucl.Tech. Vol. 157 (2007), pp. 215-229.

[2] J. Papin, B. Cazalis, J.M. Frizonnet, J. Desquines, F. Lemoine, V. Georgenthum, F. Lamare, M. Petit: Nucl.Tech.Vol. 157 (2007), pp. 230-250.

[3] F. Yunchang, D.A. Koss: Metall. Trans. A Vol. 16 (1985), pp. 675-681.

[4] M. Grange, J. Besson, E. Andrieu: Metall. Mater. Trans. A Vol. 31 (2000), pp. 679-690.

[5] S. Arsène, J.B. Bai, P. Bompard: Metall. Mater. Trans. A Vol. 34 (2003), pp. 553-566.

[6] G. Bertolino, G. Meyer, J. Perez Ipiña: J. Nucl. Mater. Vol. 320 (2003), pp. 272-279.

[7] T.M. Link, T.A. Koss, A.T. Motta: Nucl. Eng. Design Vol.186 (1998), pp. 379-394.

[8] S. Arsène, J.B. Bai, P. Bompard: Metall. Mater. Trans. A Vol. 34 (2003), pp. 579-588.

[9] J.J. Kearns: J. Nucl. Mater. Vol. 22 (1967), pp. 292-303.

[10] S. Yamanaka, D. Setoyama, H. Muta, M. Uno, M. Kuroda, K. Takeda, T. Matsuda: J. Alloys Comp. Vol. 372 (2004), pp. 129-135.

[11] N. Rupa, M. Clavel, P. Bouffioux, C. Domain, A. Legris, in: 13th International Symposium on Zirconium in the Nuclear Industry, ASTM STP 1423 (2001), pp. 811-834.

[12] M.P. Puls, S.Q. Shi, J. Rabier: J. Nucl. Mater. Vol. 336 (2005), pp. 73-80.

[13] M. Le Saux, J. Besson, S. Carassou, C. Poussard, X. Averty: J. Nucl. Mater. (2008), in press.